Investigation of the effect of air gap size on the spatial resolution in proton- and helium radio- and tomography

Stephan Radonic[1,*], **Roger A. Hälg**[1,2], **Uwe Schneider**[1,2]

[1] Department of Physics, University of Zurich, Zurich, Switzerland
[2] Radiotherapy Hirslanden AG, Rain 34, Aarau, Switzerland

Received 26 September 2019; accepted 22 March 2020

Abstract

Purpose: *Proton computed (transmission) tomography (pCT) refers to the process of imaging an object by letting protons pass through it, while measuring their energy after, and their position and (optionally) direction both before and after their traversal through that object. The so far experimental technique has potential to improve treatment planning of proton therapy by enabling the direct acquisition of a proton stopping power map of tissue, thus removing the need to obtain it by converting X-ray CT attenuation data and thereby eliminating uncertainties which arise in the mentioned conversion process. The image reconstruction in pCT requires accurate estimates of the proton trajectories. In experimental pCT detector setups where the direction of the protons is not measured, the air gap between the detector planes and the imaged object worsens the spatial resolution of the image obtained. In this work we determined the mean proton paths and the corresponding spatial uncertainty, taking into account the presence of the air gap.*

Methods: *We used Monte Carlo simulations of radiation transport to systematically investigate the effect of the air gap size between detector and patient on the spatial resolution of proton (ion) computed tomography for protons with an energy of 200 MeV and 250 MeV as well as for helium ions (He-4) with an energy of 798 MeV. For the simulations we used TOPAS which itself is based on Geant4.*

Results: *For all particles, which are detected at the same entrance and exit coordinate, the average ion path and the corresponding standard deviation was computed. From this information, the dependence of the spatial resolution on the air gap size and the angular confusion of the particle beam was inferred.*

Conclusion: *The presence of the airgap does not pose a problem for perfect fan beams. In realistic scenarios, where the initial angular confusion is around 5 mrad and for typical air gap sizes up to 10 cm, using an energy of 200 MeV a spatial resolution of about 1.6 mm can be achieved. Using protons with E = 250 MeV a spatial resolution of about 1.1 mm and using helium ions (He-4) with E = 798 MeV even a spatial resolution below 0.7 mm respectively is attainable.*

Keywords: Proton computed tomography, Monte Carlo, Proton radiography, TOPAS, Computational physics

1 Introduction

Proton radiography and tomography and the usage thereof for diagnostic purposes in medicine was investigated in the 1960s and 70s [1–5]. The development was in strong competition to the development of X-ray computed tomography (CT). Compared to X-rays, protons carry advantages as having higher density resolution while giving a lower radiation dose to the patient [6]. The main disadvantage is the worse spatial resolution which results from the multiple Coulomb scattering (MCS) of the protons in the patient [7]. One method to improve the spatial resolution is to detect the protons and reconstruct

* Corresponding author: Stephan Radonic, Radiotherapy Hirslanden, Witellikerstrasse 40, 8032 Zürich, Schweiz
E-mail: stephan.radonic@uzh.ch (S. Radonic).

Z Med Phys **32** (2022) 120–128
https://doi.org/10.1016/j.zemedi.2020.03.002
www.elsevier.com/locate/zemedi

their trajectories particle by particle, which significantly limits the image acquisition speed. Due to the ease of integration into clinical environment and substantially lower costs, X-ray CT machines have had great success and the research on proton radiography and tomography has been mostly abandoned. With the increasing number of proton treatment facilities, medical imaging with protons has regained interest. In contrast to a pure diagnostic use, also the suitability of proton radiography and tomography as a quality assurance tool for proton therapy was evaluated [8].

Currently proton therapy treatment planning is typically based on X-ray CT imaging. The acquired X-ray attenuation map has to be converted into a proton stopping power map. However the physical interactions of protons and photons while traversing matter are fundamentally different, leading to potential inaccuracies [9,10]. Proton computed tomography (pCT) on the other hand directly acquires a proton stopping power map and thus could remove this uncertainty. Additionally proton computed radiography could also be applied to verify the correct delivery of the proton treatment plan before or after the treatment. With the increasing availability of advanced detector technology, high-speed data acquisition systems and vast amounts of processing power, pCT has great potential to further improve proton therapy [11].

For the image reconstruction of proton radio- and tomographies, estimates of the proton paths are necessary. In literature various estimates are used, ranging from straight lines connecting the measured entrance and exit points up to cubic spline estimates and advanced analytical MCS models. For pCT setups where the direction (angle) of the protons is not being measured before and after their traversal through the imaged object, the air gap decreases the spatial resolution, as has been shown in two prior studies [12,13]. In the study by Schneider et al. [12] the impact of a 5 cm air gap before and behind the imaged object, on the spatial resolution was studied with Monte Carlo methods for 200 MeV protons. Krah et al. [13] used analytical methods to study the impact of various detector setups, energies and air gap sizes on the spatial resolution of proton beams. Their analytical results were verified with Monte Carlo simulations for a single energy and air gap size. In this study the impact of air gap on spatial resolution was also studied for helium ions. In addition the variation of spatial resolution for different air gap sizes was studied as a function of the angular confusion of the beam, as we are also interested in the possibility of using large initial angular confusions for imaging. For our study Monte Carlo methods were used, because it includes also the treatment of nuclear interactions as well as single and plural coulomb scattering.

2 Materials and methods

Monte Carlo based particle transport simulations are used to simulate the behaviour of protons traversing a water box, which is used as an approximation for tissue. Basically the simulation consists of shooting a large number of protons through a water box and obtaining their trajectories through phase-space scoring. In the post-processing analysis the detector setup is assumed to be a tracker setup without angle measurements. The parameter space of air gap size and angular confusion was chosen such that it resembles typical clinical setups, as well as that the possibility of using a large angular confusion for imaging is explored.

2.1 TOPAS and Geant4

For the simulation of the proton tomography the *TOPAS* (Tool for particle simulation) package was used, which itself is based on the well known Monte Carlo radiation transport code *Geant4*, developed by CERN. *TOPAS* wraps the *Geant4* Toolkit and lets the user configure all the properties of the simulation like geometry, particle source, physics and scoring setup through a single parameter (text) file. This drastically simplifies the creation of simulation scenarios [14].

Geant4 is an advanced Monte Carlo method based package for the simulation of particle traversal and interactions in matter. It is implemented in the C++ programming language and is designed on modern software engineering methodologies [15].

2.2 Physics

Geant4 provides various physics models for different purposes. For the simulations done in the context of this paper the default physics list which TOPAS provides is used. According to the TOPAS guide it has been shown to work well for proton therapy research [14].

2.3 Geometry

The setup was chosen to consist of a $5 \times 5 \times 5$ m sized vacuum filled box which represents the "simulation world". The simulation world holds a $1.2 \times 1.2 \times 1.2$ m large air box. Inside it a 20 cm × 40 cm × 40 cm sized water box is placed, which represents the phantom. A proton beam source is placed at the z-origin of the air box in the center of its x-y plane. The phantom (water box) inside is placed adjacent to the beam source, its position on the z-axis can be varied to enclose an air gap between itself and the beam source. In the simulations the enclosed air gap is varied between 0 and 30 cm by varying the z-position of the water box. At an interval of 1 mm on the z-axis the airbox is intersected with scoring planes, which themselves are x-y planes residing in a "parallel" simulation world and have no influence on the physical simulation. When a proton traverses such a scoring plane, its physical parameters as position, angle, energy as well as its id are written into an output file. This geometrical setup is depicted in Figure 1, the enclosing vacuum box representing the simulation world is not shown in the figure.

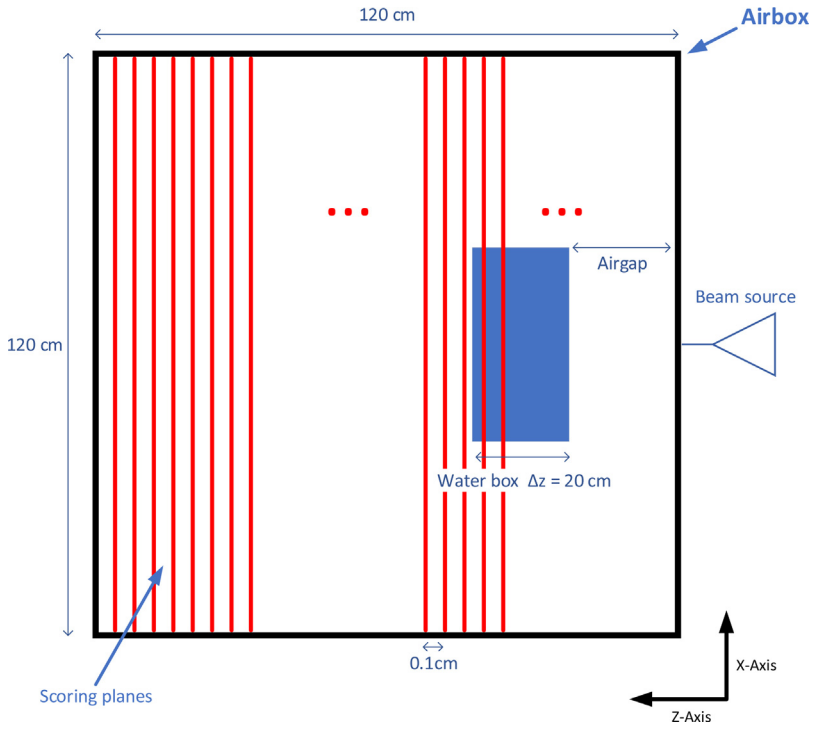

Figure 1. Schematic overview of the geometric setup of the simulation in *TOPAS*, the enclosing vacuum box representing the simulation world is not shown in the figure.

2.4 Beam source

We use simulated beams of protons with an energy of $E = 200$ MeV and $E = 250$ MeV as well as beams of $He-4$ ions with an energy of $E = 798$ MeV. The energy values were chosen large enough such that typical patient sizes can be imaged, but not too large, because spatial resolution typically increases with increasing energy. The beams were set up with Gaussian angular distributions with angular confusion values ranging between 0 mrad, which corresponds to a perfect fan beam, up to 100 mrad, which is a fairly large angular confusion in the context of particle beams used for radio-therapeutic applications. It is further assumed that the beams have no position distribution and no energy spread. The energy value of 798 MeV for the $He-4$ ions is chosen such that the range of the $He-4$ ions in waters matches the range of the 200 MeV protons, which is approximately $R = 26.2$ cm.

The number of protons in the simulation is set to 100,000. In order to have good statistics for the data analysis a large enough amount of particles is needed. Setting this number higher (e.g. 1 million particles) would provide even better statistics, but the amount of data generated also increases tenfold, which would pose a major obstacle for data analysis, which is explained in detail in the next section.

2.5 Simulation output data

The simulation scoring is configured such that as ions traverse the scoring planes (see also Section 2.3), their current physical properties are being written into an output file. In this context it should be noted that secondary fragments were excluded from the analysis. In experimental setups this could be achieved using a filter acting on the energy loss of the particles. We have a scoring plane every millimetre across the z-axis of the airbox, which in total makes 1200 scoring planes. In terms of data size of the output data which need to be processed, this yields ≈3.4 Gigabytes for the output of a single simulation run. As with each variation of the simulation parameters as air gap, angular confusion, energy, etc. the simulation has to be rerun and the data analysis needs to be repeated, the amount of data which has to be processed, grows rather quickly. In our case it reached a total size of over *1 terabyte*.

2.6 Process

In a first step the simulation output file is read into memory and the records are stored into an unordered array. Then the records are sorted into bunches according to their *Event ID*, so that a bunch contains all the records belonging to the corresponding proton trajectory. Also from the unordered array

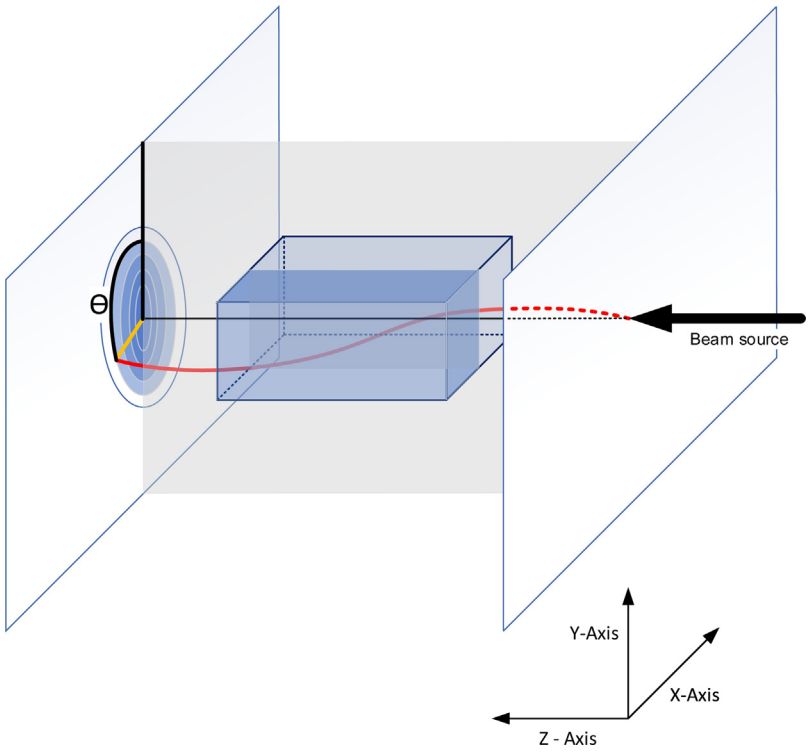

Figure 2. 3D schematic of the simulation geometry for better understanding of the data analysis process.

we obtain all the records whose z-coordinate belong to the scoring plane, which is assumed to be the exit detector.

Next, using the exit plane data, the proton trajectories are assigned to bins according to the radius ($r^2 = x^2 + y^2$) of their exit point. We set the bin size to 0.1 mm which corresponds to assuming a "perfect" pixel detector with a resolution of $0.1/\sqrt{12}$ mm. (see also Figure 2) Due to homogeneity and isotropy of the scattering process the x and y axes are interchangeable and it is therefore physically allowed to rotate all radii vectors of a particular trajectory through a constant angle around the x-axis. We want that after the transformations (rotations) the exit points of all trajectories at the detector plane lie along the same line (in the z-y plane at $x = 0$). For this purpose we obtain the angles θ enclosed between the line at $x = 0$ where the z-y Plane intersects the exit scoring (x-y) plane and the radius vectors of the exit points. Then we iterate through all trajectory points contained in each bunch, and apply the rotation matrix M_{rot} (Eq. (1)) with the angle corresponding to the trajectory of that particular bunch, obtained in the previous step, to the radius vector of each point.

$$M_{\text{rot}} = \begin{pmatrix} \cos(\theta) & -\sin(\theta) \\ \sin(\theta) & \cos(\theta) \end{pmatrix} \tag{1}$$

With that, the reconstruction of the proton trajectories from the simulation output data is finished and the obtained single proton trajectories can be used for further analysis.

We want to obtain the mean proton path as well as the standard deviation of the trajectories from the mean proton path, which corresponds to the spatial resolution. For that purpose the proton trajectories were previously assigned to bins. Iterating through all bins, *for each z-coordinate* in a first step we calculate the average x and y coordinates of all protons assigned to the current bin, and in a second step using the obtained average coordinates we compute the average as well as the standard deviation of the radius

$$(\bar{r})_i = \sqrt{\bar{x}^2 + \bar{y}^2} \tag{2}$$

$$(\sigma_r)_i = \frac{1}{N_i} \sum_{k=0}^{N_i} \sqrt{(x_k - \bar{x})^2 + (y_k - \bar{y})^2} \tag{3}$$

where i is the iteration over the bins, and k is iteration over the particles contained in the particular bin. Having obtained σ_r for each z-coordinate for all bins, these values are used to compute the weighted average of σ_r over all bins as in Eq. (4), where i is the iteration variable over all bins as before. The weighing factor w_i equals the number of particles inside the

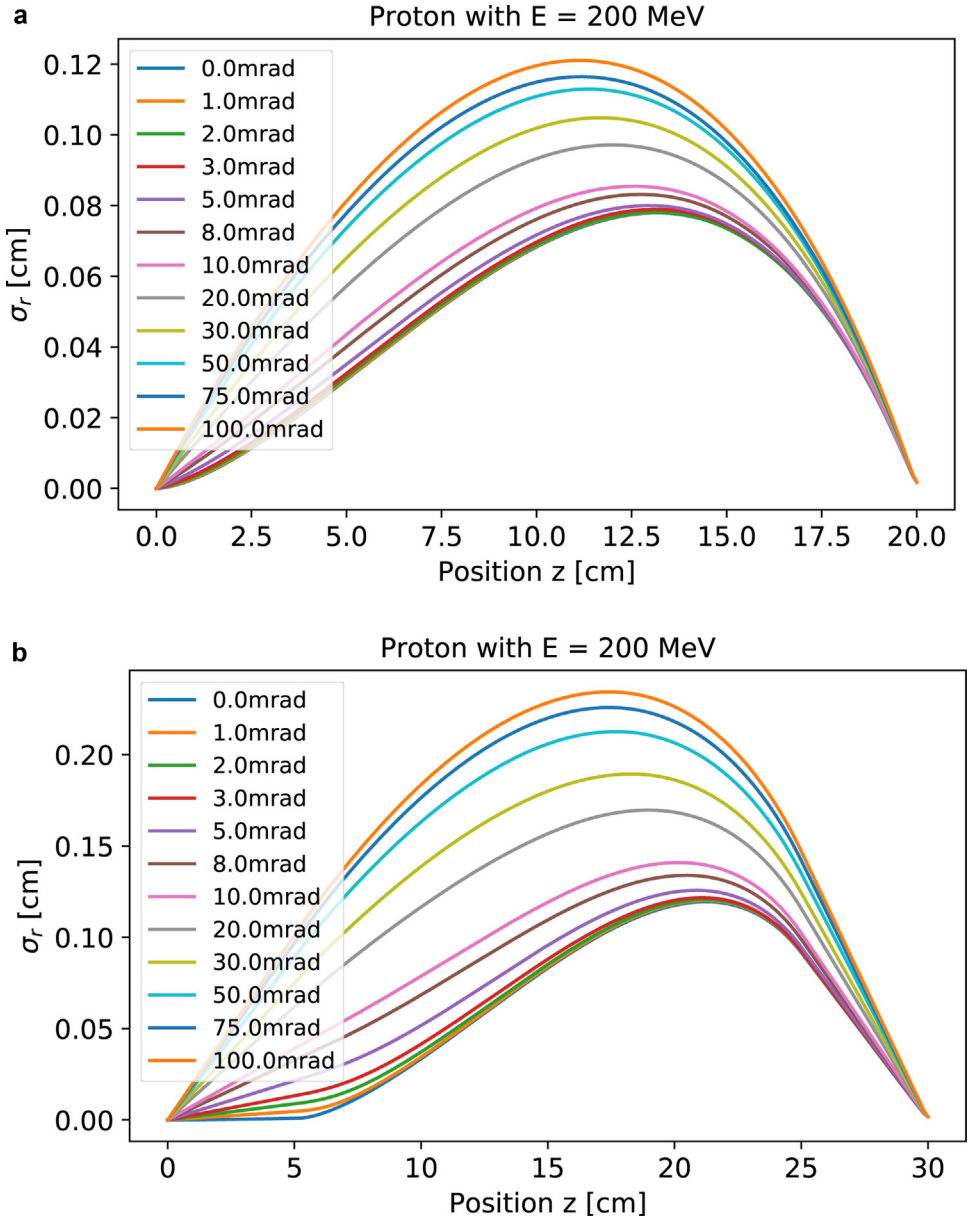

Figure 3. Spatial uncertainty of proton radiography with proton energy $E = 200$ MeV for multiple initial angular confusions (the ordering of the curves is the same as the label order) A: without air gap; B: with an symmetrical air gap of 5 cm between phantom and the detector planes.

particular bin i. This yields the spatial uncertainty at a position on the z-axis.

$$\sigma_r(z) = (\overline{\sigma_r})_z = \frac{\sum_{i=0}^{N_{\text{bins}}} \left((\sigma_r)_z\right)_i w_i}{\sum_{i=0}^{N_{\text{bins}}} w_i} \tag{4}$$

Finally the obtained data is written into output files.

2.7 Implementation and optimization

The amount of data which has to be processed (see Section 2.5) requires an efficient implementation of the analysis routines, so that the processing does not take too long and thus the flexibility of being able to quickly reprocess the data in case of modifications to the analysis

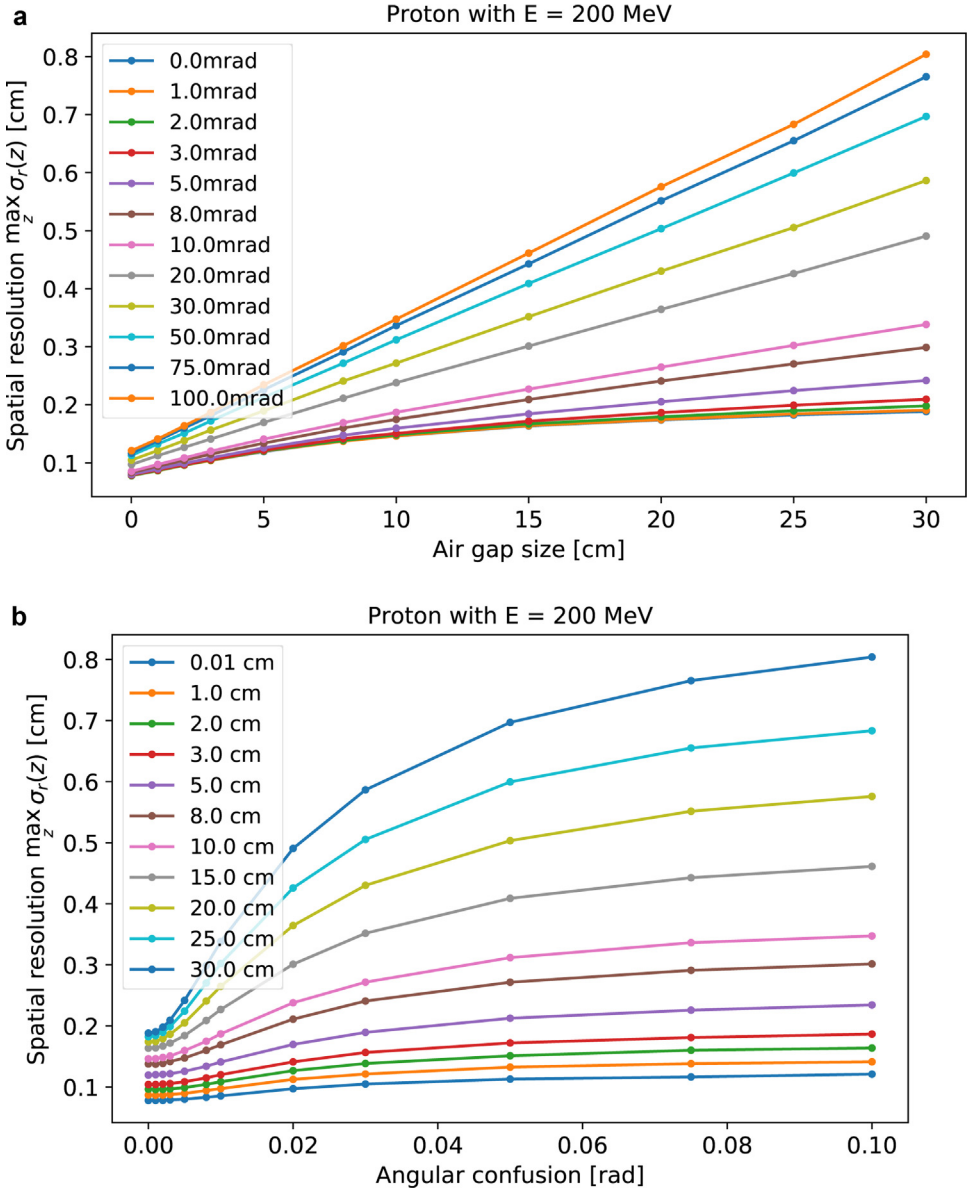

Figure 4. Spatial resolution of proton radiography with proton energy $E = 200$ MeV (the order of the curves is the same as the label order) A: depending on the symmetrical air gap size between phantom and the detector planes for multiple initial angular confusions; B: depending on the initial angular confusion for multiple constant symmetrical air gap sizes between phantom and the detector planes.

procedure, is provided. The data analysis routine was implemented in the *C++* programming language, which is very well suited for high performance and throughput. In the data analysis routine explained in Section 2.6 there were two particular suitable computing intensive parts, that we tackled with parallelization and vectorization, which are common high performance computing (HPC) techniques.

3 Results

Using the data analysis procedures depicted in Section 2.6 on the simulation output data, we obtained the spatial uncertainty of proton radiography using proton beams with an energy of $E = 200$ MeV and $E = 250$ MeV as well as for heavy ions (He-4) with $E = 798$ MeV. In Figure 3a the spatial uncertainty for various initial angular confusions is plotted as a

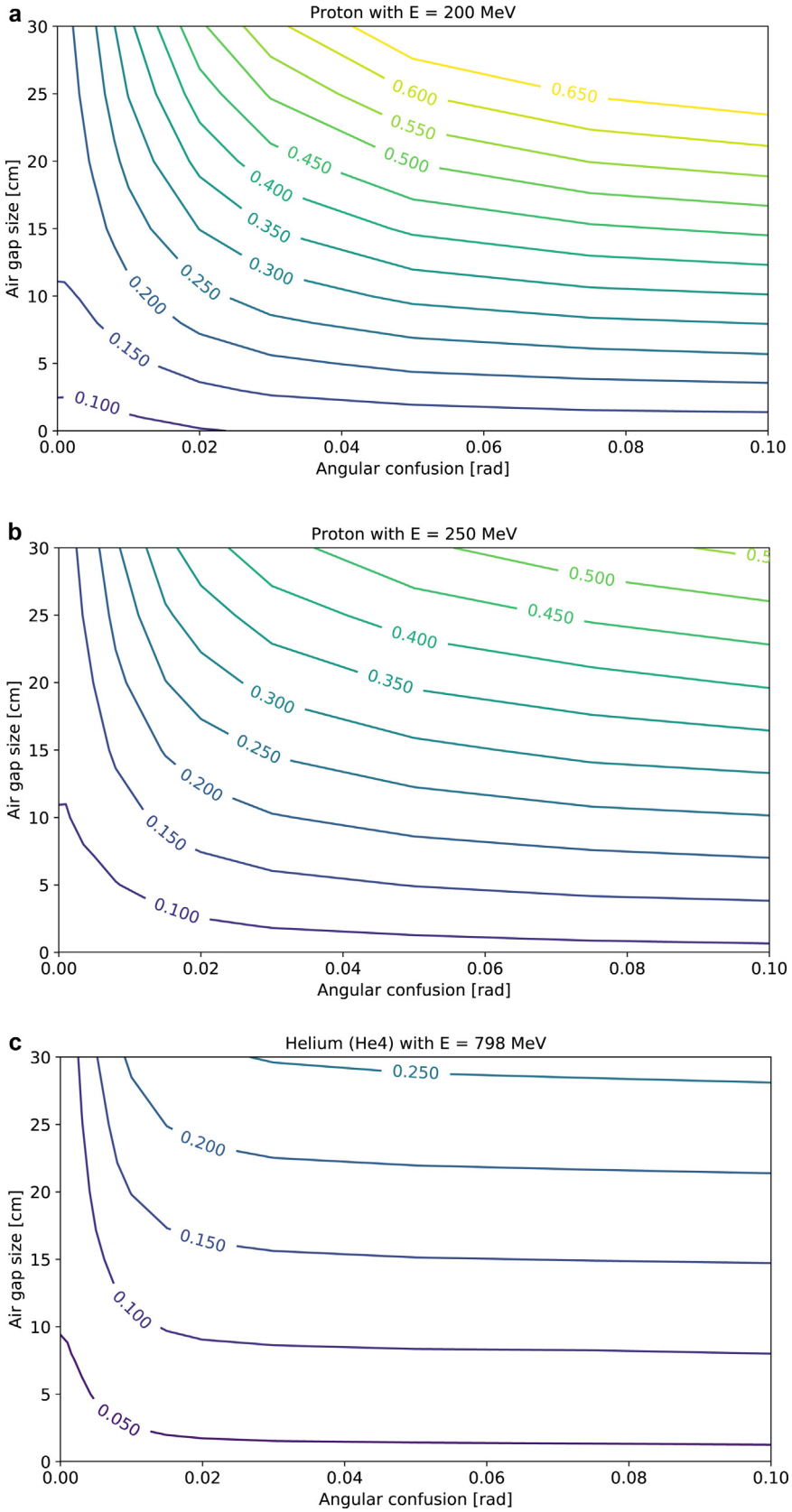

Figure 5. Isoline contour plot of spatial resolution (in cm) of ion radiography depending on the symmetrical air gap size between phantom and the detector planes and the initial angular confusions A: protons with energy $E = 200$ MeV; B: protons with energy $E = 250$ MeV; C: helium ions with energy $E = 798$ MeV.

function of the position on the z-axis. Comparing that with Figure 3b where there is a symmetrical 5 cm air gap in front and after the phantom it can be easily seen the air gap increases the spatial uncertainty, the increase being proportional to the initial angular confusion. What also can be noticed is that the position of the maximal spatial uncertainty shifts from the end of the phantom towards its centre.

To further explore the dependence of the spatial resolution, which corresponds to the maximal spatial uncertainty $\max \sigma_r(z)$, on the initial angular confusion of the beam and the symmetrical air gap size between detector planes in front and after the phantom in Figure 4a and b the maximal spatial uncertainty is plotted as a function of the initial angular confusion and air gap size respectively. The points are the actual values for the maximal spatial uncertainty from the simulations whereas the connecting lines are interpolations between those points. For initial angular confusions up to approximately 10–20 mrad the spatial resolution decreases non linearly with increasing air gap size. For higher initial angular confusion values the dependence is fairly linear. In dependence of the angular confusion the spatial resolution up decreases linearly, the slope being dependent on the air gap size, after a threshold being approximately at 20 mrad, the decrease saturates and >50 mrad the spatial resolution remains almost constant with increasing angular confusion. The isoline contour plot in Figure 5a provides a particularly insightful view on the dependence of spatial resolution on both parameters in a single plot.

The same analysis has also been done for protons with $E = 250$ MeV and for the heavy *He-4* ions with $E = 798$ MeV. With the higher beam energy the spatial uncertainty though decreases thus allowing larger values for initial angular confusion and air gap size. Using *He-4* ions the spatial resolution improves even further. The general observations of the functional dependence of spatial resolution on air gap size and initial angular confusion which were already made for protons of $E = 200$ MeV still hold.

4 Discussion and conclusion

The results of systematical simulation-based investigations of the impact of an air gap of equal size between entrance and exit detector planes and the phantom on the spatial resolution of proton and heavy ion radiography have been presented in Section 3. Assuming an air gap of equal size in front and after the phantom is motivated by tomography scenarios where the detector setup is being rotated around the imaged object. The clinical requirement on spatial resolution is in the order of a millimeter. The Gantry-2 proton beam at the PSI treatment facility for example has an initial angular confusion σ_{ini} of approximately 5 mrad for energies above 200 MeV. The air gap size in a proton tomography scenario can be assumed to be about 10 cm. With these parameters at a beam energy of 200 MeV a spatial resolution of about 1.6 mm can be achieved. At a beam energy of 250 MeV a spat. resolution of about 1.1 mm is attainable. Using Helium (He-4) ions with an energy of $E = 798$ MeV matching the range in water of 200 MeV protons, the spatial resolution is even <0.7 mm. If the initial angular confusion is assumed to be 10 mrad, the maximum air gap size which with it is possible to achieve a spatial resolution of 1 mm, is only about 2 cm at $E = 200$ MeV and 5 cm at $E = 250$ MeV. It can be concluded that the usage of the highest available proton beam energy (at proton treatment facilities) or the usage of heavy ions allow some discretion in terms of initial phase space and air gap size while achieving acceptable spatial resolution. Helium ions could possibly even allow the usage of a large initial angular confusion (>100 mrad) with an air gap size of 10 cm while still achieving a spatial resolution of 1.2 mm (see Figure 5c). Assuming a tracker detector setup this could potentially be used to minimize the number of radiography image acquisitions at different angles necessary for a full tomography. If a non parallel proton beam is used for imaging, the image content of the irradiation from a fixed angle results not only in a projectional image, but in three dimensional information about the object. If an iterative backprojection algorithm is used, it is possible to simultaneously reconstruct images in different depths of the patient. The advantage of this method is an improved spatial resolution as described in [16]. This would lead to reconstruction methods where less acquisitions at different angles are necessary.

The data obtained in this work could be used in the context of detector development, as well as for validation and benchmarking of analytical models. The most likely proton paths could also be used for image reconstruction.

Conflicts of interest

The authors declare no conflicts of interest.

References

[1] Koehler AM. Proton radiography. Science 1968;160(3825):303–4, http://dx.doi.org/10.1126/science.160.3825.303 http://science.sciencemag.org/content/160/3825/303, ISSN 0036-8075.
[2] Steward VW, Koehler AM. Proton beam radiography in tumor detection. Science 1973;179(4076):913–4, http://dx.doi.org/10.1126/science.179.4076.913 http://science.sciencemag.org/content/179/4076/913, ISSN 0036-8075.
[3] Moffett DR, Colton EP, Concaildi GA, Hoffman EW, Klem RD, Knott MJ, et al. Initial test of a proton radiographic system. IEEE Trans Nucl Sci 1975;22(June (3)):1749–51, http://dx.doi.org/10.1109/TNS.1975.4327982. ISSN 0018-9499.
[4] Hanson KM, Bradbury JN, Cannon TM, Hutson RL, Laubacher DB, Macek RJ, et al. Computed tomography using proton energy loss. Phys Med Biol 1981;26(6):965 http://stacks.iop.org/0031-9155/26/i=6/a=001.
[5] Hanson KM, Bradbury JN, Koeppe RA, Macek RJ, Machen DR, Morgado R, et al. Proton computed tomography of human specimens. Phys Med Biol 1982;27(1):25 http://stacks.iop.org/0031-9155/27/i=1/a=003.
[6] Schulte RW, Bashkirov V/, Márgio C, Klock L, Li T, Wroe AJ, et al. Density resolution of proton computed tomography. Med Phys 2005;32(4):1035–46, http://dx.doi.org/10.1118/1.1884906.
[7] Schneider U, Pedroni E, Hartmann M, Besserer Jürgen, Lomax T. Spatial resolution of proton tomography: methods, initial

phase space and object thickness. Z Med Phys 2012;22(2):100–8, http://dx.doi.org/10.1016/j.zemedi.2011.06.001. ISSN 0939-3889, http://www.sciencedirect.com/science/article/pii/S093938891100064X.

[8] Schneider U, Pedroni E. Proton radiography as a tool for quality control in proton therapy. Med Phys 1995;22(4):353–63, http://dx.doi.org/10.1118/1.597470.

[9] Schneider U, Pedroni E, Lomax A. The calibration of ct hounsfield units for radiotherapy treatment planning. Phys Med Biol 1996;41(1):111 http://stacks.iop.org/0031-9155/41/i=1/a=009.

[10] Sadrozinski HFW, Bashkirov V, Keeney B, Johnson LR, Peggs SG, Ross G, et al. Toward proton computed tomography. IEEE Trans Nucl Sci 2004;51(February (1)):3–9, http://dx.doi.org/10.1109/TNS.2003.823044. ISSN 0018-9499.

[11] Schulte R, Bashkirov V, Li T, Liang Z, Mueller K, Heimann J, et al. Conceptual design of a proton computed tomography system for applications in proton radiation therapy. IEEE Trans Nucl Sci June 2004;51(3):866–72, http://dx.doi.org/10.1109/TNS.2004.829392. ISSN 0018-9499.

[12] Schneider U, Besserer Jürgen, Hartmann M. Technical note: spatial resolution of proton tomography: impact of air gap between patient and detector. Med Phys 2012;39(2):798–800, http://dx.doi.org/10.1118/1.3676739.

[13] Krah N, Khellaf F, Létang JM, Rit S, Rinaldi I. A comprehensive theoretical comparison of proton imaging set-ups in terms of spatial resolution. Phys Med Biol 2018; 63(13):135013.

[14] Perl J, Shin J, Schümann J, Faddegon B, Paganetti H. Topas: an innovative proton monte carlo platform for research and clinical applications. Med Phys 2012;39(11):6818–37, http://dx.doi.org/10.1118/1.4758060. ISSN 2473-4209.

[15] Agostinelli S, Allison J, Amako K, Apostolakis J, Araujo H, Arce P, et al. Geant4-a simulation toolkit. Nucl Instrum Methods Phys Res Sect A: Accel Spectrom Detect Assoc Equip 2003;506(3):250–303, http://dx.doi.org/10.1016/S0168-9002(03)01368-8. ISSN 0168-9002, http://www.sciencedirect.com/science/article/pii/S0168900203013688.

[16] Schneider U. Proton radiography. A tool for quality control in proton therapy. PhD thesis, ETH Zurich, Zürich, 1994. Diss. Naturwiss. ETH Zürich, Nr. 10780, Ref.: Max Anliker; Korref.: Peter Rüegsegger; Korref.: Eros Pedroni; 1994.